Point and line defects in checkerboard patterned hybrid nematic films: A computer simulation investigation

Mariana Casaroto,[1] Cesare Chiccoli,[2] Luiz Roberto Evangelista,[1,3] Paolo Pasini,[2] Rodolfo Teixeira de Souza,[1,3,*] Claudio Zannoni,[4] and Rafael Soares Zola[1,3]

[1]*Departamento de Física, Universidade Estadual de Maringá, Avenida Colombo, 5790-87020-900 Maringá, Paraná, Brazil*

[2]*INFN, Sezione di Bologna, Via Irnerio 46, 40126 Bologna, Italy*

[3]*Departamento Acadêmico de Física, Universidade Tecnológica Federal do Paraná, Campus Apucarana, Rua Marcílio Dias, 635 CEP 86812-460–Apucarana, Paraná, Brazil*

[4]*Dipartimento di Chimica Industriale "Toso Montanari", Università di Bologna, Viale Risorgimento 4, I-40136 Bologna, Italy*

(Received 18 October 2023; accepted 20 June 2024; published 19 July 2024)

We consider a nematic liquid crystal film confined to a flat cell with homeotropic and planar patterned hybrid anchoring and show, using Monte Carlo simulations, the possibility of the system to stabilize line and point defects. The planar anchoring surface is patterned with a chessboardlike grid of squares with alternating random or parallel homogeneous planar anchoring. The simulations show only line defects when the individual domains are small enough, but also point defects when the domain size is significantly larger than the sample thickness. In the latter case, defect lines are not observed in domains with random surface anchoring, although lines and points are connected by a thick line which separates two regions with different director tilts. Increasing the anchoring strength, the defect lines appear a few layers above the surface, with the two ends just above the randomly oriented domains.

DOI: 10.1103/PhysRevE.110.014704

I. INTRODUCTION

Liquid crystals (LCs) [1–3] are anisotropic fluids well-known in everyday life for flat panel displays [4,5], with applications continuing to expand in different fields from organic electronics [6,7], biosensors, and bioengineering [8–11] to stimuli controlled actuators [12–14] and many more [15,16], even if the relation between molecular structure and properties is still far from being fully understood. Some of these technologies also depend not only on the existence of orientational molecular order with respect to a local preferred direction (director) but also on singularities of the director field (defects) that show up in the optical textures of LC thin films observed between crossed polarizers [1,17]. In nematic liquid crystals (NLCs), defects are observed after a phase transition when cooling from the isotropic phase, as the sample relaxes trying to reduce its free energy and, correspondingly, defects tend to spontaneously annihilate [18]. However, defects can be stabilized, e.g., in thin films or capillaries, by employing suitable boundary conditions. The possibility of directly observing topological defects [19–21] in controlled experimental conditions [22] is of great general interest as their universal features allow employing LCs as a laboratory for observations of relevance in fields as diverse as superfluidity or cosmology [18,23,24].

As the name would seem to suggest, defects are normally undesirable for the operation of electro-optical devices and displays based on nematic liquid-crystalline materials, where they can decrease the image quality, even if they can also increase the response in displays based on cholesteric blue phases, where the defects lines are well organized [25,26].

In any case, it is important to note that topological defects can add or modify some properties and functions of ordered soft materials. This is particularly relevant for liquid crystals due to their susceptivity to external stimuli [2,3], and in view of the fact that certain defects can be created and stabilized by a combination of surface geometry and boundary conditions [25,27], as in the case of nematics confined to spherical or cylindrical containers [1] or to thin films [28]. The rapidly developing field of defect engineering aims to control and, in special cases, create or eliminate defects providing templates for the fabrication of complex material organizations [25, 29–33]. The development of experimental techniques based on surface chemical treatments [34] or, perhaps more conveniently, on light exposure of photo-sensitive aligning materials [35], opened the possibility of producing samples with a variety of patterned surface for applications in areas such as electro-optic devices or stimuli responsive actuators [36], among others [35]. Surface patterns can be inscribed on the surface plates to promote anchoring in diverse ways [37–39] and, for instance, induce defects [27] or bistability [40,41]. Recently, techniques to create patterns on surfaces to induce arbitrary anchoring have been used to stabilize complex networks of disclination lines [32,42,43].

Predicting or even understanding the intricacies of defect formation for complex geometries and anchoring conditions is of obvious importance but can be particularly challenging

*Contact author: rodolfosouza@utfpr.edu.br

 ©2024 American Physical Society

for analytic-type theories, and thus computer simulations can be particularly handy as an alternative or complementary approach to continuum-type modeling [44]. In fact, Monte Carlo (MC) simulations of lattices of interacting headless spins [3] have long been successfully used to simulate complex structures [45], topological lines, and point defects [20,46–50]. In the case of a thin film with hybrid boundary alignment (homeotropic anchoring on one surface and strong and planar degenerate on the other), such boundaries were shown to be crucial for producing and maintaining the experimentally observed defects [51]. Extensive work has been done on defect simulation of hybrid films using lattice models, showing good agreement with continuum modeling and experiments where these are available [52–56]. The point defects were found to be located on the random surface, with the spins lying perpendicular to the surfaces in their core region. This model was extended to nematic with elastic anisotropy [53], where it was observed that half-integer point defects can emerge by setting suitable elastic constants, and also with biaxial nematics [28,56]. On the other hand, defect lines are supposed to appear in hybrid films with the planar surface offering uniform alignment [28]. Recently, the effects of the elastic constants in such defect lines were studied in depth [55], while a few years ago experiments and computer simulations were successfully performed with the aim of studying the transition between points to lines defects by increasing the disorder of the planar anchoring surface [54].

Here, our main aim is to observe both types of defects together in the same sample and investigate how they interact with each other. This task is performed by computationally building a sample with the planar alignment patterned as a chessboard with the alternating square domains endowed with uniform and random anchoring, respectively. We analyze the structures with textures and isosurface visualizations which permit us to examine how the defects are connected. The effects of size domains and anchoring strength are investigated.

The paper is organized as follows. In the next section, we describe the sample, the simulation method, and the visualization techniques. In Sec. III, the results are reported and discussed and some concluding remarks are presented in Sec. IV.

II. THE SIMULATION MODEL

A set of $N + N_S$ headless spins are placed at the sites of a cubic lattice of dimensions $L \times L \times (h+2)$, mimicking a square film, with thickness h, confined between two flat boundary layers, in which N represents the number of spins in the volume and N_s represents the number of spins on the surface. Referring to the laboratory frame of reference, the boundary plates are positioned at $z = 0$ and $z = h + 1$ with normal parallel to $\hat{z}$. The orientation of the $L \times L$ spins on the bottom surface, $\mathcal{S}_{\rm bot}$ (at $z = 0$) and on the top one, $\mathcal{S}_{\rm top}$ (at $z = h + 1$), are set to impose the anchoring conditions and are kept fixed throughout the simulation. The N spins placed on each of the inside bulk layers, $\mathcal{B}$, are free to rotate in any direction. By considering the orientation of the ith spin as

$$\mathbf{u_i} = u_{ix}\mathbf{x} + u_{iy}\mathbf{y} + u_{iz}\mathbf{z}, \tag{1}$$

we set the spins on $\mathcal{S}_{\rm top}$ with $u_{iz} = 1$ and $u_{ix} = u_{iy} = 0$, corresponding to a perfect homeotropic alignment. The bottom surface, $\mathcal{S}_{\rm bot}$ on the other hand, corresponds to a patterned planar alignment with squares of random and aligned domains. The planar random domain is built by setting $u_{iz} = 0$, and u_{ix} and u_{iy} random numbers ranging from -1 to 1, with $u_{ix}^2 + u_{iy}^2 = 1$, while the planar aligned domains are built by setting $u_{ix} = 1$ and $u_{iy} = u_{iz} = 0$. The pattern can then be viewed as a chessboardlike grid with arbitrary $n \times n$ domains, with $n > 2$ and even, where the simulated patterned surface offers both kinds of alignment side by side: planar degenerated and uniform.

The Hamiltonian of this system is given by

$$H = \frac{1}{2}\sum_{\substack{i,j\in\mathcal{B}\\ i\neq j}} \Phi_{ij} + J_{\rm bot}\sum_{\substack{i\in\mathcal{B}\\ j\in\mathcal{S}_{\rm bot}}} \Phi_{ij} + J_{\rm top}\sum_{\substack{i\in\mathcal{B}\\ j\in\mathcal{S}_{\rm top}}} \Phi_{ij}, \tag{2}$$

where the parameters $J_{\rm bot}$ and $J_{\rm top}$ model the anchoring strength at the bottom and top surfaces. The attractive pair potential Φ_{ij} is the Gruhn-Hess-Romano-Luckhurst one [53,54,57–59],

$$\begin{aligned}\Phi_{ij} = \epsilon_{ij}\{&\lambda[P_2(\mathbf{u}_i\cdot\mathbf{s}_{ij}) + P_2(\mathbf{u}_j\cdot\mathbf{s}_{ij})]\\ &+ \mu[(\mathbf{u}_i\cdot\mathbf{s}_{ij})(\mathbf{u}_j\cdot\mathbf{s}_{ij})(\mathbf{u}_i\cdot\mathbf{u}_j) - 1/9]\\ &+ \nu P_2(\mathbf{u}_i\cdot\mathbf{u}_j) + \rho[P_2(\mathbf{u}_i\cdot\mathbf{s}_{ij}) + P_2(\mathbf{u}_j\cdot\mathbf{s}_{ij})]P_2(\mathbf{u}_i\cdot\mathbf{u}_j)\},\end{aligned} \tag{3}$$

with the strength of the pair interaction $\epsilon_{ij} = \epsilon$ if i and j are nearest neighbors, and 0 otherwise, and $\mathbf{s}_{ij} = \mathbf{r}/|\mathbf{r}|$, $\mathbf{r} = \mathbf{r_i} - \mathbf{r_j}$, with $\mathbf{r_i}$, $\mathbf{r_j}$ the position vectors of the ith and jth lattice points. Simulations are performed at a reduced temperature T_R, $T_R = k_BT/\epsilon$, with k_B the Boltzmann constant and T the absolute temperature. The potential parameters are a combination of the splay, twist, and bend Frank elastic constants, K_1, K_2, K_3, respectively, and are written as [53,54,57,58]

$$\lambda = \tfrac{1}{3}\Lambda(2K_1 - 3K_2 + K_3), \tag{4a}$$

$$\mu = 3\Lambda(K_2 - K_1), \tag{4b}$$

$$\nu = \tfrac{1}{3}\Lambda(K_1 - 3K_2 - K_3), \tag{4c}$$

$$\rho = \tfrac{1}{3}\Lambda(K_1 - K_3), \tag{4d}$$

where Λ is a length related to the dimension of the unit cell [59]. Finally, P_2 is the well-known second rank Legendre polynomial. Such potential has proved particularly useful in describing elastic properties of nematics in a variety of situations [3]. If all the elastic constants are set to be equal, then Eq. (2) reduces to the Lebwhol-Lasher pair potential [60], which has been successfully employed to describe the nematic-isotropic phase transition (occurring at $T_R \approx 1.1232$ in the bulk [61,62]) and to investigate the orientational order in nematic liquid crystals [59].

The spins of the bulk have their starting alignment parallel to the z direction. Such an initial condition (IC) mimics a configuration in which the material is completely oriented by a strong external electrical or magnetic field. Alternatively, random initial conditions, mimicking a fast quenching from an isotropic phase, can also reproduce some of the results presented here. The cell is updated with the classic Monte Carlo (MC) Metropolis algorithm [63] with the orientations of

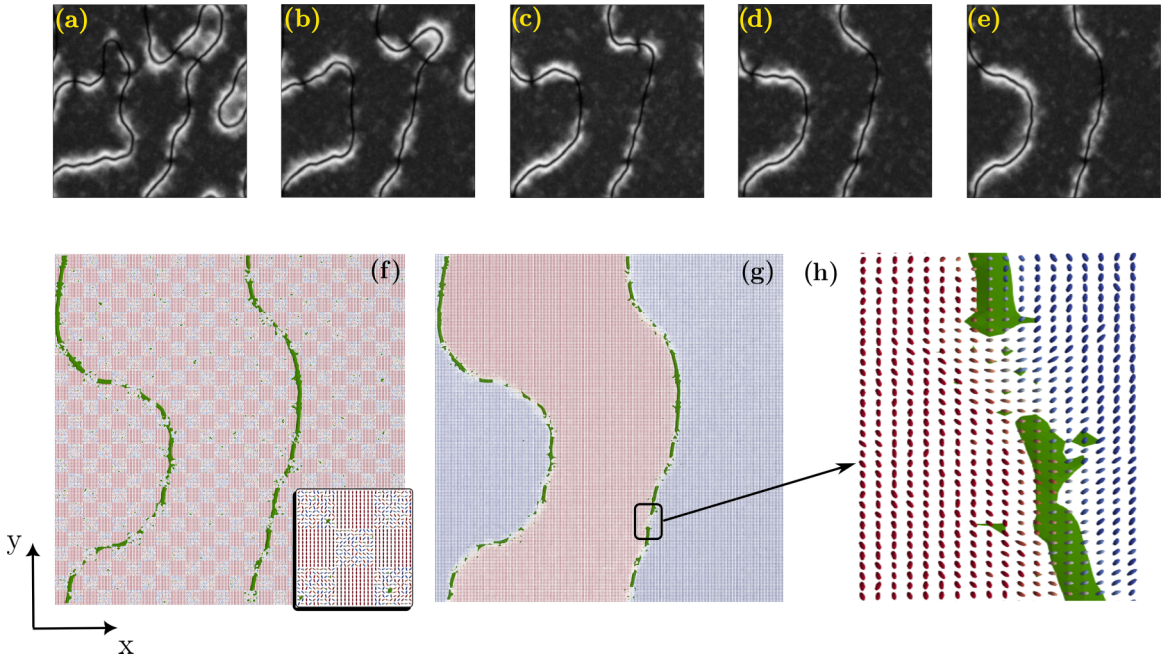

FIG. 1. (a)–(e) MC evolution from 10 000, 20 000, 30 000, 40 000, and 50 000 MCCs of the POM texture for a cell with alternating domains of size 10×10 ($n = 24$). In (f), we plot the order parameter isosurface for a threshold of $S = 0.76$ at 50 000 MCCs superimposed to the patterned surface and with the snapshot of the first layer above the support surface. Each spin is colored according to its u_{ix} component (plotting the $-\mathbf{u}_\mathbf{i}$ if $u_z < 0$, when necessary) from blue ($u_{ix} = -1$) to red ($u_{ix} = +1$), so the x-aligned square domains in (f) appear red, while the random domains present spins of this whole range of color. In (h), we show in detail the marked region in (g) to exhibit the spins configurations of the defects, highlighting in green the defect regions, where the spins are vertically oriented, and the defectless regions, where the spins vary continuously from the region with positive to negative x component.

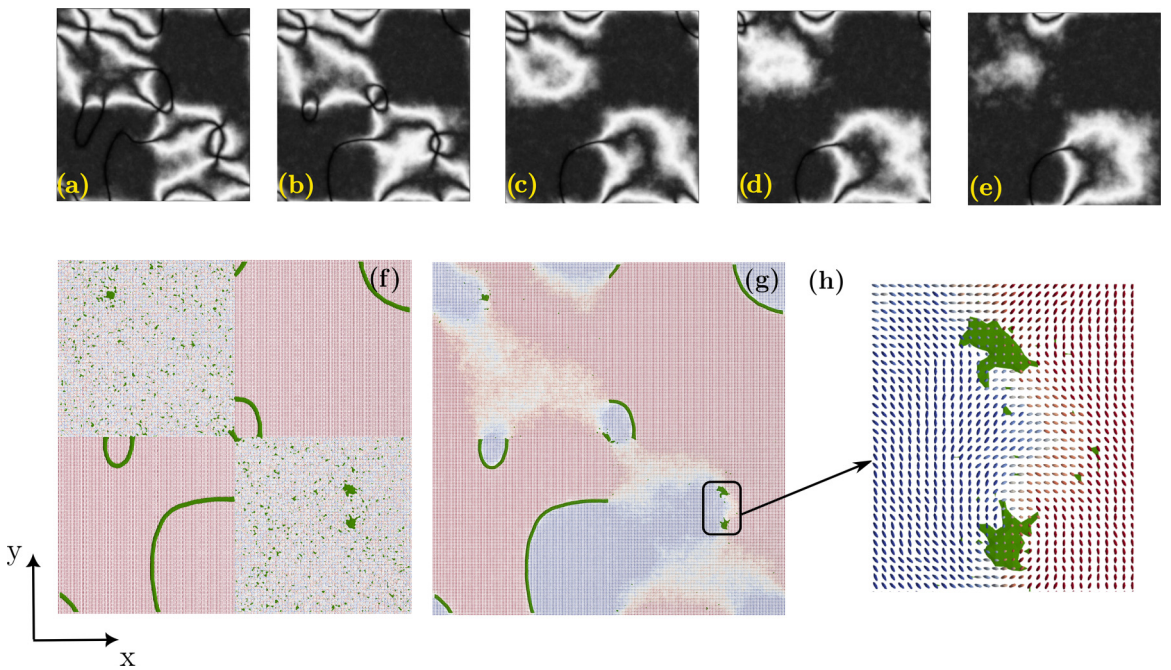

FIG. 2. Images of the 2×2 grid sample with $J_{\text{bot}} = J_{\text{top}} = 0.5$, with the optical textures at (a) 10 000, (b) 20 000, (c) 30 000, (d) 40 000, and (e) 50 000 MCCs. (f), (g) Isosurfaces and snapshots of bottom boundary conditions and the first layer of free spins, respectively, for the sample with 20 000 MCCs. The region with a pair of ± 1 defects, marked in (g) is expanded in (h). The color code is the same as that used in the previous figure.

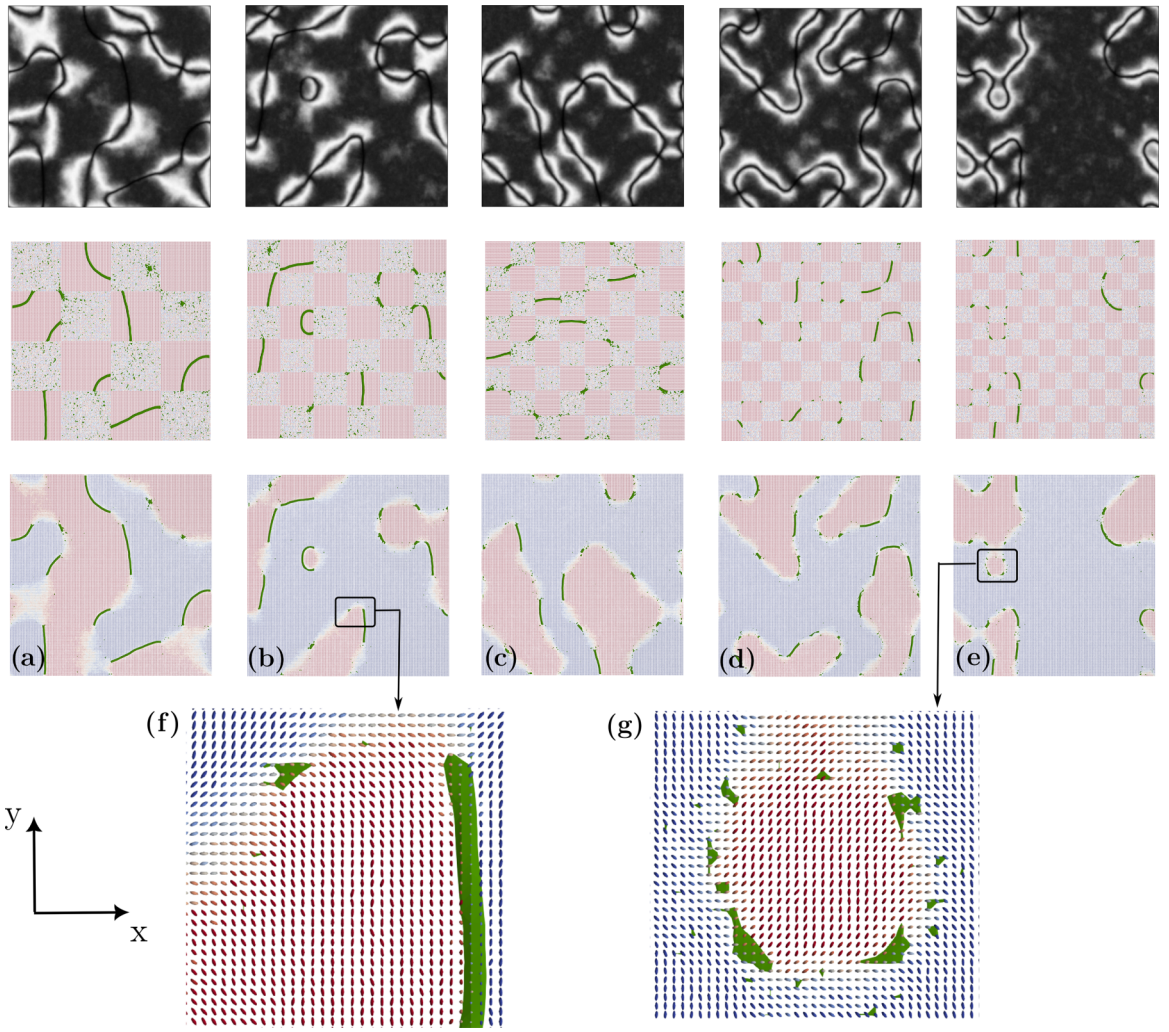

FIG. 3. In each column, set of textures, snapshots, and isosurfaces for $n = 4$(a), 6 (b), 8(c), 10 (d), and 12 (e) for $J_{\text{bot}} = J_{\text{top}} = 0.5$. (f), (g) Close-up of the region delimited by the rectangles in (b) and (e), respectively.

each spin generated with the Barker-Watts technique [64]. A Monte Carlo cycle is defined as a set of N of these individual attempted updates, with N the number of spins inside the cell, as defined above. The configurations of the spins after a certain number of MC cycles (MCCs) can be investigated by using some different techniques. One of them is simply through snapshots, i.e., direct views of the spins. These can directly supply information about how each spin and its surroundings are organized, but snapshot of 3D arrangements are difficult to use to identify any structure due to the high number of particles in an image. Then, with the aim of studying topological defects, it is useful to complement a snapshot of spin layers with an isosurface of some suitable parameter able to locate such defects. In our paper, we use the local order parameter S_i to identify them. S_i is evaluated as the largest eigenvalue of the 3×3 ordering matrix [3] with elements

$$Q^i_{jk} = \left\langle \tfrac{1}{2}(3u_{ij}u_{ik} - \delta_{j,k}) \right\rangle, \tag{5}$$

with u_{ij} and u_{ik} being the jth and kth components of the ith spin, and the average is evaluated over the set of nearest neighbors, as well as on Monte Carlo cycles. In addition to these techniques, an excellent way to analyze the microscopic organizations is by simulating polarized optical microscopy (POM) experiments that show the optical textures between crossed polarizers. We built them by using the Müller matrix procedure, which is described in detail, e.g., in Ref. [3]. Here, we employ the set of optical parameters: light wavelength of $\lambda = 545$ nm, LC material ordinary and extraordinary refractive indices $n_o = 1.5$ and $n_e = 1.66$, respectively, and virtual layer separation length of $h = 0.53$ μm.

III. SIMULATIONS AND RESULTS

We have run simulations for a box of $L \times L \times (h + 2)$ spins at a fixed temperature $T_R = 0.1$ well inside the ordered phase. As for the set of elastic constants, we choose to use values of a typical liquid crystals as 5CB with the splay, twist, and bend constants $K_1 = 7.0$ pN, $K_2 = 4.4$ pN, and $K_3 = 9.7$ pN [65]. The bottom surface was divided into $n \times n$ domains, with n an even number, so as to comply with periodic boundary conditions. We have kept the box size fixed to $240 \times 240 \times (10 + 2)$ and used $n = 2$, 4, 6, 8, 10, 12, and 24, corresponding to individual domain sizes $\ell \times \ell$, with $\ell =$ 120, 60, 40, 30, 20, 12, and 10.

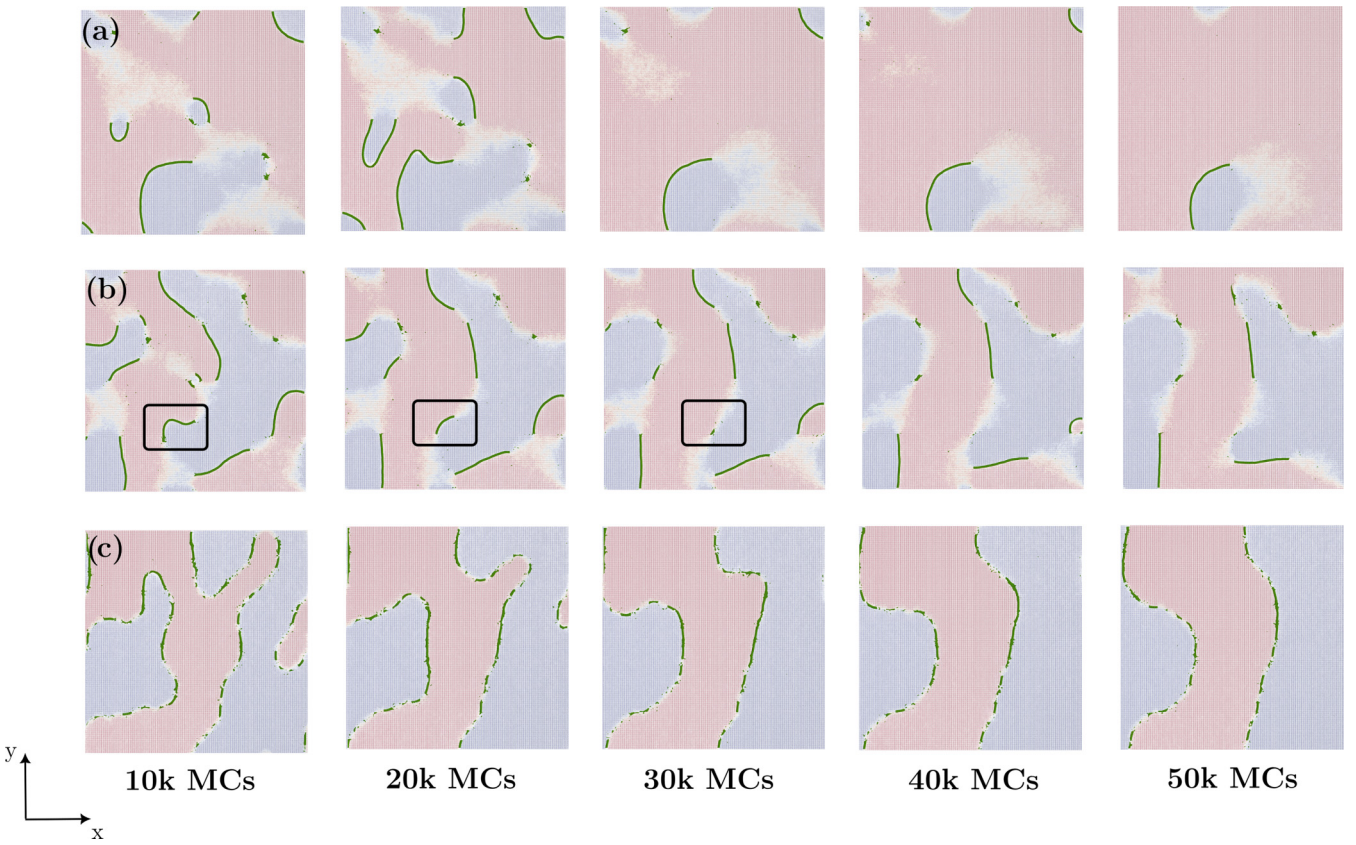

FIG. 4. MC evolution for samples with $J_{bot} = J_{top} = 0.5$ and $n = 2$ (a), 4 (b), and 12 (c), showing how defect lines relax after 10 000, 20 000, 30 000, 40 000, and 50 000 MCCs and, eventually, vanish.

We start by presenting our results for the smallest individual square cell (10×10, with $n = 24$) and an anchoring strength of $J_{bot} = J_{top} = 0.5$. The simulated POM textures and some snapshots are shown in Fig. 1.

In Figs. 1(a)–1(e), we can visualize the evolution of the textures during the first 50 000 MCCs. Isosurfaces were built and, in Fig. 1(f), they were superimposed to the patterned plate, while in Fig. 1(g), they were drawn over the snapshot of the first layer, where they are, in fact, placed. The isosurfaces shown here and in the other figures correspond to a threshold of $S = 0.76$. We can see from these figures only defect lines, which indicates that only defects with $\pm 1/2$ topological charge are formed. Due to the initial vertical alignment boundary condition, the spins in the bulk have, initially at least, large z and small x and y components. This alignment is favored close to the top surface due to the homeotropic anchoring condition. When the alignment predominant at the bottom surface is parallel to the x direction, the spins close to this surface tend to align to this direction. However, the free energy presents a degeneracy on the directions x and $-x$, then the spins tend with equal probability to one of these directions. From the IC, and influenced by the homeotropic surface, the spins in bulk can acquire a component in the x direction, u_x, lying to $+x$ or $-x$, according to their neighborhood. Eventually, a spin can acquire a negative z component, and we can plot its direction flipped, which is more common with random (IC). Since the energy of interaction of a spin parallel to z with a spin with components $\mathbf{u} = \pm u_x \mathbf{x} + \sqrt{1 - u_x^2}\mathbf{z}$ depends on an even function of u_x, both signs represent equal energy states. Hence, some regions of the sample will be dominated by an alignment with component x positive, and others with x negative. At the boundaries of the two regions, $u_x \to 0$ and a defect line emerges, corresponding to spins with a $u_z \to 1$ component. Then, such degenerescence of both states is the main aspect for the line defect formation in hybrid cells as treated here [56]. The color palette employed here allows us to distinguish a $+x$ (red) from a $-x$ (blue) component of the spin. In Fig. 1(f), the red squares correspond to the homogeneously aligned domains. It is interesting to note that, despite some discontinuity, the defect lines are present above regions with both kinds of anchoring. Since the random domains are fairly small, the overlayer presents an alignment along x sufficient to promote the formation and stabilization of the defect line, which is present in the whole sample. In some discontinuities, as the one emphasized on the zoomed in area shown in Fig. 1(h), the spins seem to lie on a plane xy, different from what happens on the defect, characterized by a line of spins with a high z component.

On the other hand, in the case of the largest (120×120) domains studied here (which corresponds to $n = 2$), shown in the set of images in Fig. 2, it is possible to notice both point and line defects.

Hence, random and aligned domains can be easily identified in Fig. 2(f). In this case, we can see that the defect lines are not connected to each other, as can be seen in the isosurface map. However, by performing an analysis of the regions

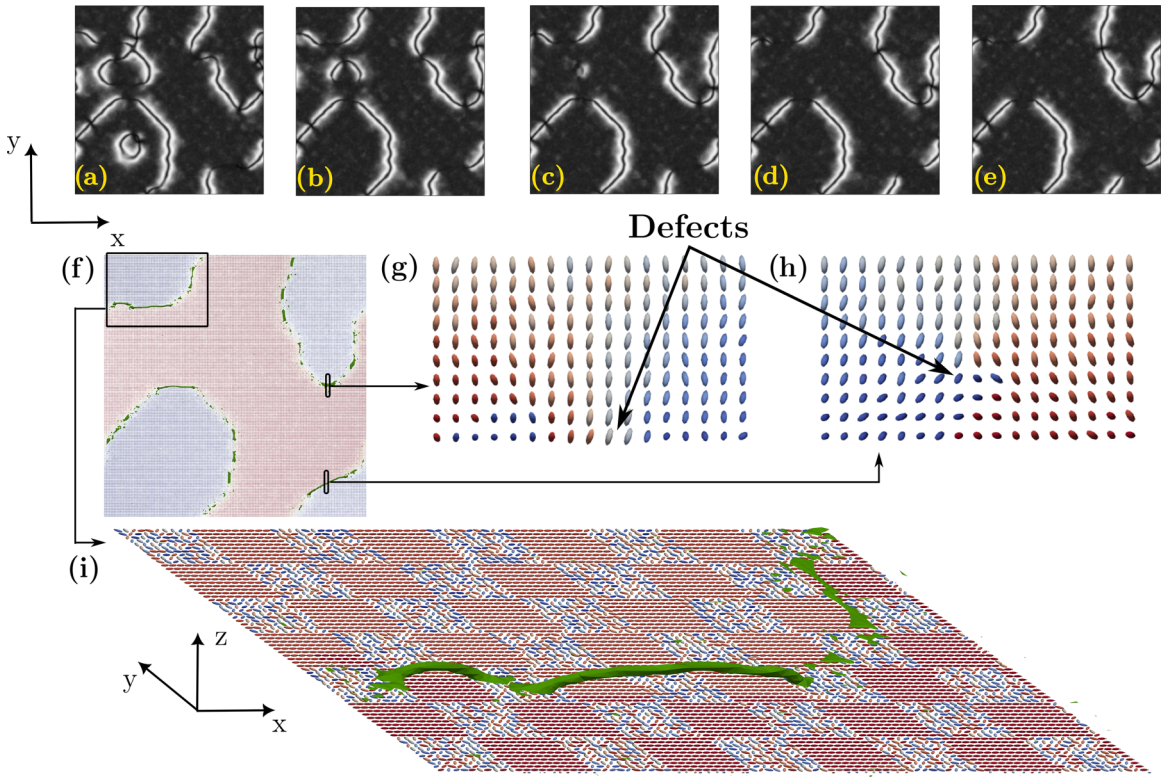

FIG. 5. Evolution of the sample with $J_{bot} = 0.7$ and $J_{top} = 0.5$ and $n = 24$ from 10 000 MCCs (a) to 50 000 MCCs (e) in steps of 10 000 MCCs. (f) Snapshot of the fifth layer of free spins above the patterned surface. The regions marked by dotted lines in (f) showing the defect positions shown in (*g*) and (*h*). (i) 3D view of the order isosurface for the small region marked in the top left of (f), showing how some defects leave the surface plane while others still lie on it.

of $+x$ and $-x$ orientations on the first layer, as suggested by the textures shown in Fig. 2(g) and by the zoomed-in region in Fig. 2(h), it seems that all the defects, lines, and points are, somehow, linked by the regions with $\pm x$ spins components. This can be seen, for instance, from the region between the defect line and the pair of point defects on the bottom right side of this image.

By analyzing the effect of domain size on the formation and topological charges of defects, it is expected that point defects should not be observed in small domains. In fact, our simulations indicate that this kind of defect can be observed only for grids with cells larger than 40×40 spins ($n = 6$). For $n = 8$ (30×30 size), the sample presents only line defects. This feature can be observed in Fig. 3, where we show the textures, snapshots, and isosurfaces for $n = 4, 6, 8, 10$, and 12. The line defects for these analyzed values of n are located exclusively on the portion of an aligned domain, and normally both ends are placed in random domains. The case of $n = 12$, i.e., of grid cells 20×20 presented in Fig. 3(e), sometimes tends to show a small region of line defects on a random alignment domain, but in the relaxation process the lines tend to avoid the regions above such random domains.

On the process of defect annihilation and its speed, we note that for the present system, point defects tend to disappear before lines, at least on the larger domains. Point defects annihilate in pairs, as seen in the bottom right portion of the textures in Figs. 2(a)–2(c) and their snapshots in Fig. 4(a), or the defects moves towards the region where the bottom surface offers a uniform alignment anchoring, as seen in the defect placed in the top left portion of that sample. Here, it is possible to see in the texture, in the center of Fig. 2(a), what seems a point defect, with the four brushes typical of the Schlieren texture. However, by looking at the snapshot with the help of a map of isosurfaces, it becomes clear that it is instead a small line defect, as shown in Fig. 2(f). Line defects, in turn, tend to close themselves to annihilate, and some lines persist for very long runs, as can be seen in the left bottom and top right portion of textures [Figs. 2(a)–2(c) and 4(a)]. This is the case also observed in the cell with the smallest grid size. The line defects persist after a high number of Monte Carlo cycles, as shown in Fig. 4(c).

In Fig. 4(b), we show the relaxation process of the $n = 4$ sample. Here we highlight another interesting feature: the boundary between regions of spins with $+x$ and $-x$ components appears to be smoothed in some points, allowing the defect line to vanish by dismantling, at both ends, the line of high z component spins in its core. This is emphasized by the black squares on the images. In our simulations, we observe this behavior with the intermediate values of lattice size n studied, showing some influence of the random alignment on the line defect annihilation. Such an aspect is not observed for the largest grid size, where the influence is negligible and they are almost independent, and for the smallest, where this influence does not seem to be strong enough. On the other hand, it is interesting to note that the pair of point defects located in the top right region of Fig. 4(b), which are on neighboring

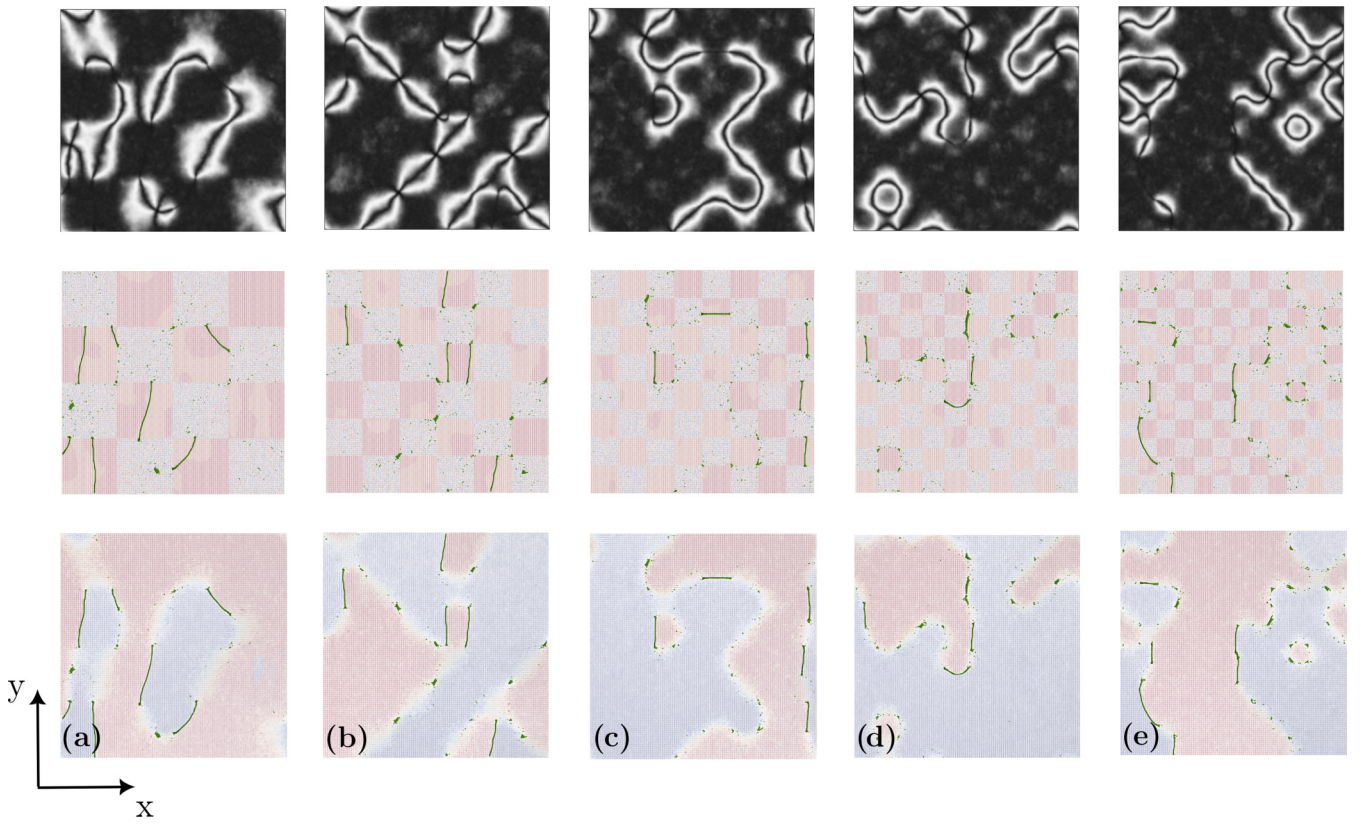

FIG. 6. The effects of size domain on defect line position for $n = 4$ (a), 6 (b), 8 (c), 10 (d), and 12 (e), with $J_{\text{bot}} = 0.7$ and $J_{\text{top}} = 0.5$. Defects completely placed on the surface as, for instance, those marked in last line, are observed in (d) and (e), although in all values, the small line in the domain corner are also placed in surface. Defects placed above the surface, in the bulk, are observed in all values of n.

random domains, as can also be seen in the bottom image of Fig. 3, still persists even after 50 000 MCCs.

Let us now focus our attention on the effect of anchoring strength at the two surfaces. It is clear that increasing the anchoring intensity at the top surface will increase even more the z component of the spins close to it, i.e., homeotropic alignment, and we expect no relevant changes on the results already reported. The situation is rather different, however, when changing the anchoring strength at the bottom surface and the effects are visible from the textures and in the snapshots shown in Figs. 5 and 6. By carefully looking at the textures, it is possible to note some dark lines among brighter lines. An example of these lines can be seen in the top left corner of Fig. 5(a) and its time evolution up to that at 50 000 MCCs shown in Fig. 5(e). Note that the brighter lines are connected by dark ones. It is easier to see in Fig. 5(f), which corresponds to the snapshot of Fig. 5(e), that in these regions there are defect lines. Both lines, dark and bright, present a special difference. They are lines of $\pm 1/2$ defects but placed in different regions. While for the brighter lines, as in the cases reported until now, the lines lie in the first layer above the surface, as shown in Fig. 5(g), in the darker lines the defect is found around four layers above the surface, i.e., in the bulk, as can be seen in Fig. 5(h). When the anchoring is stronger, the spins close to the bottom surface tend to sustain their planar alignment in a small region of the bulk closest to the surface, even influencing the spins above of random domains. In Fig. 5(i), we show a 3D view of the isosurfaces on the alignment domains in the bottom surface. In this image, it is possible to see that when the line escapes towards the bulk, the end lines appear to be placed on random domains.

Turning now to examine how the grid cell size can affect the defects, we show in Fig. 6 the texture and snapshots with isosurfaces for $n = 4$, 6, 8, 10, and 12. Point defects are still observed only up to $n = 6$ (lateral size $\ell = 40$ lattice points). Defect lines can be observed closer to surfaces for higher values of n, as highlighted in Figs. 6(d) and 6(e), although some small lines located on the corner of the domains also lie on the surface and can be viewed for the entire range on n. The defect lines for lower values of n are characterized by being placed above the surface, mainly on the fourth layer above surface, with both of their ends placed exactly on the random alignment domain.

IV. DISCUSSION AND CONCLUDING REMARKS

We considered a nematic liquid crystal film confined to a flat cell with homeotropic and planar-patterned hybrid anchoring, similar to a chessboard pattern, with alternating square domains featuring uniform and random anchoring, respectively. By employing Monte Carlo simulations, we have been able to demonstrate the system's capability to stabilize line and point defects. We have observed that the interplay between domain size, anchoring conditions, and system size plays a crucial role in determining the types of defects that emerge. For smaller domain sizes (up to 40×40 spins),

point defects with $\pm 1/2$ topological charge can be observed alongside line defects, while for larger domains, we only observe line defects at the domain corners. Point defects tend to annihilate in pairs or move towards regions with uniform alignment anchoring. Line defects, on the other hand, tend to persist for longer simulation times and can even close themselves to annihilation. Anchoring strength at the bottom surface has a significant influence on defect behavior. Stronger anchoring leads to the formation of defect lines deeper in the bulk of the system rather than just at the surface. These deeper defects are characterized by being located several layers above the surface and can be connected to surface-aligned domains.

In conclusion, our extensive simulations of liquid crystal systems within different domain sizes and anchoring strengths have provided valuable insights into the formation and behavior of topological defects. In particular, our findings give us a clear picture of how defects form and behave in liquid crystal systems, helping us understand how different factors influence defect behavior. These findings should be valuable for designing and manipulating liquid crystal systems for various applications from displays to advanced materials.

ACKNOWLEDGMENTS

The authors thank the National Council for Scientific and Technological Development (CNPq), the Coordination for the Improvement of Higher Education Personnel (CAPES). This paper was partially supported by the National Institute of Science and Technology Complex Fluids—INCT-FCx (R.S.Z. and L.R.E.), and the São Paulo Research Foundation (FAPESP No. 2014/50983-3). R.S.Z. thanks CNPq (No. 304634/2020-4). Research developed with support of LAMAP-UTFPR.

[1] P. G. de Gennes and J. Prost, *The Physics of Liquid Crystals* (Oxford University Press, Oxford, 1995).
[2] I. C. Khoo, *Liquid Crystals*, 3rd ed. (Wiley, New York, 2022).
[3] C. Zannoni, *Liquid Crystals and their Computer Simulations* (Cambridge University Press, Cambridge, 2022).
[4] J. H. Lee, D. N. Liu, and S. T. Wu, *Introduction to Flat Panel Displays* (Wiley, Chichester, 2008).
[5] D. A. Yakovlev, V. G. Chigrinov, and H.-S. Kwok, *Modeling and Optimization of LCD Optical Performance* (Wiley, Chichester, 2015).
[6] M. O'Neill and S. M. Kelly, Ordered materials for organic electronics and photonics, Adv. Mater. **23**, 566 (2011).
[7] R. De and S. K. Pal, Self-assembled discotics as molecular semiconductors, Chem. Commun. **59**, 3050 (2023).
[8] A. M. Lowe and N. L. Abbott, Liquid crystalline materials for biological applications, Chem. Mater. **24**, 746 (2012).
[9] Y.-Y. Luk, Liquid crystals and nanostructured surfaces: A novel system for detecting protein-binding events, J. A. Schwarz and C. I. Contescu, editors, in *Dekker Encyclopedia of Nanoscience and Nanotechnology* (Dekker, New York, 2004), pp. 1635–1646.
[10] P. V. Shibaev, M. Wenzlick, J. Murray, A. Tantillo, and J. Howard-Jennings, Rebirth of liquid crystals for sensoric applications: Environmental and gas sensors, Adv. Cond. Matter Phys. **2015**, 8 (2015).
[11] B. Gurboga, E. B. Tuncgovde, and E. Kemiklioglu, Liquid crystal-based elastomers in tissue engineering, Biotechnol. Bioeng. **119**, 1047 (2022).
[12] Y. Y. Xiao, Z. C. Jiang, J. B. Hou, X. S. Chen, and Y. Zhao, Electrically driven liquid crystal network actuators, Soft Matter **18**, 4850 (2022).
[13] P. Zhang, L. T. de Haan, M. G. Debije, and A. Schenning, Liquid crystal-based structural color actuators, Light: Sci. & Appl. **11**, 248 (2022).
[14] M. O. Saed, A. Gablier, and E. M. Terentjev, Exchangeable liquid crystalline elastomers and their applications, Chem. Rev. **122**, 4927 (2022).
[15] J.-P. F. Lagerwall and G. Scalia, A new era for liquid crystal research: Applications of liquid crystals in soft matter nano-, bio- and microtechnology, Current Appl. Phys. **12**, 1387 (2012).
[16] H. K. Bisoyi and Q. Li, Liquid crystals: Versatile self-organized smart soft materials, Chem. Rev. **122**, 4887 (2022).
[17] P. M. Chaikin and T. C. Lubensky, *Principles of Condensed Matter Physics* (Cambridge University Press, Cambridge, 1995).
[18] H. Mukai, P. R. G. Fernandes, B. F. de Oliveira, and G. S. Dias, Defect-antidefect correlations in a lyotropic liquid crystal from a cosmological point of view, Phys. Rev. E **75**, 061704 (2007).
[19] M. Kleman, *Points, Lines and Walls: in Liquid Crystals, Magnetic Systems and Various Ordered Media* (Wiley, New York, 1982).
[20] O. D. Lavrentovich, P. Pasini, C. Zannoni, and S. Žumer, *Defects in Liquid Crystals: Computer Simulations, Theory and Experiments* (Kluwer, Dordrecht, 2001).
[21] M. Kleman and O. D. Lavrentovich, *Soft Matter Physics* (Springer, Berlin, 2003).
[22] N. D. Mermin, The topological theory of defects in ordered media, Rev. Mod. Phys. **51**, 591 (1979).
[23] T. W. B. Kibble, Topology of cosmic domains and strings, in *Cosmological Constants*, edited by J. Bernstein and G. Feinberg (Columbia University Press, New York, 1986), p. 277.
[24] R. Repnik, A. Ranjkesh, V. Simonka, M. Ambrozic, Z. Bradac, and S. Kralj, Symmetry breaking in nematic liquid crystals: Analogy with cosmology and magnetism, J. Phys.: Condens. Matter **25**, 404201 (2013).
[25] T. Araki, F. Serra, and H. Tanaka, Defect science and engineering of liquid crystals under geometrical frustration, Soft Matter **9**, 8107 (2013).
[26] H. Kikuchi, M. Yokota, Y. Hisakado, H. Yang, and T. Kajiyama, Polymer-stabilized liquid crystal blue phases, Nat. Mater. **1**, 64 (2002).
[27] M. Kralj, M. Kralj, and S. Kralj, Topological defects in nematic liquid crystals: Laboratory of fundamental physics, Phys. Status Solidi A **218**, 2000752 (2021).
[28] M. Buscaglia, G. Lombardo, L. Cavalli, R. Barberi, and T. Bellini, Elastic anisotropy at a glance: The optical signature of disclination lines, Soft Matter **6**, 5434 (2010).
[29] M. Grzelczak, J. Vermant, E. M. Furst, and L. M. Liz-Marzan, Directed self-assembly of nanoparticles, ACS Nano **4**, 3591 (2010).

[30] M. A. Gharbi, M. Nobili, and C. Blanc, Use of topological defects as templates to direct assembly of colloidal particles at nematic interfaces, J. Colloid Interface Sci. **417**, 250 (2014).

[31] A. Jangizehi, F. Schmid, P. Besenius, K. Kremer, and S. Seiffert, Defects and defect engineering in soft matter, Soft Matter **16**, 10809 (2020).

[32] Y. Guo, M. Jiang, S. Afghah, C. Peng, R. Selinger, O. D. Lavrentovich, and Q. H. Wei, Photopatterned designer disclination networks in nematic liquid crystals, Adv. Opt. Mater. **9**, 2100181 (2021).

[33] M. J. Shin and D. K. Yoon, Role of stimuli on liquid crystalline defects: From defect engineering to switchable functional materials, Materials **13**, 5466 (2020).

[34] R. A. Drawhorn and N. L. Abbott, Anchoring of nematic liquid-crystals on self-assembled monolayers formed from alkanethiols on semitransparent films of gold, J. Phys. Chem. **99**, 16511 (1995).

[35] V. Chigrinov, A. Kudreyko, and Q. Guo, Patterned photoalignment in thin films: Physics and applications, Crystals **11**, 84 (2021).

[36] I. Nys, Patterned surface alignment to create complex three-dimensional nematic and chiral nematic liquid crystal structures, Liq. Cryst. Today **29**, 65 (2020).

[37] J. P. Bramble, S. D. Evans, J. R. Henderson, C. Anquetil, D. J. Cleaver, and N. J. Smith, Nematic liquid crystal alignment on chemical patterns, Liq. Cryst. **34**, 1059 (2007).

[38] D. Lysenko, P. Pagliusi, C. Provenzano, Y. Reznikov, K. Slyusarenko, and G. Cipparrone, Periodic defects lines in liquid crystal cell guided by polarization holograms at an aligning surface, Appl. Phys. Lett. **103**, 151913 (2013).

[39] C. Anquetil-Deck, D. J. Cleaver, J. P. Bramble, and T. J. Atherton, Independent control of polar and azimuthal anchoring, Phys. Rev. E **88**, 012501 (2013).

[40] C. Anquetil-Deck, D. J. Cleaver, and T. J. Atherton, Competing alignments of nematic liquid crystals on square-patterned substrates, Phys. Rev. E **86**, 041707 (2012).

[41] T. Araki and J. Nagura, Bistable director alignments of nematic liquid crystals confined in frustrated substrates, Phys. Rev. E **95**, 012706 (2017).

[42] T. Ouchi, K. Imamura, K. Sunami, H. Yoshida, and M. Ozaki, Topologically protected generation of stable wall loops in nematic liquid crystals, Phys. Rev. Lett. **123**, 097801 (2019).

[43] M. F. Wang, Y. N. Li, and H. Yokoyama, Artificial web of disclination lines in nematic liquid crystals, Nat. Commun. **8**, 388 (2017).

[44] G. Barbero and L. R. Evangelista, *An Elementary Course on the Continuum Theory for Nematic Liquid Crystals* (World Scientific, Singapore, 2001).

[45] R. L. Biagio, R. T. de Souza, L. R. Evangelista, R. R. Ribeiro de Almeida, and R. S. Zola, Spontaneous striped pattern formation in thin chiral nematic liquid crystal layers, J. Mol. Liq. **269**, 703 (2018).

[46] C. Chiccoli, P. Pasini, F. Semeria, T. J. Sluckin, and C. Zannoni, Monte Carlo simulation of the hedgehog defect core in spin systems, J. Phys. II France **5**, 427 (1995).

[47] C. Chiccoli, I. Feruli, O. D. Lavrentovich, P. Pasini, S. Shyianovskii, and C. Zannoni, Monte Carlo simulations of topological defects in Schlieren textures of biaxial and uniaxial nematic liquid crystals, Phys. Rev. E **66**, 030701(R) (2002).

[48] E. K. Omori, G. H. X. Masso, R. L. Biagio, L. R. Evangelista, R. Teixeira de Souza, and R. S. Zola, Monte Carlo simulations of chiral and achiral nematic droplets: Thermal quenches and role of the elastic constants, Liq. Cryst. **50**, 1392 (2023).

[49] R. L. Biagio, R. T. Souza, L. R. Evangelista, and R. S. Zola, Frustrated structures and pattern formation after thermal quenches in cholesteric liquid crystal droplets, J. Mater. Chem. C **9**, 8623 (2021).

[50] E. K. Omori, R. S. Zola, and R. Teixeira de Souza, Stable disclination lines in nematic liquid crystals confined in thin films with periodic-planar surfaces: A Monte Carlo study, J. Mol. Liq. **342**, 117538 (2021).

[51] O. D. Lavrentovich and Y. A. Nastishin, Defects in degenerate hybrid aligned nematic liquid crystals, Europhys. Lett. **12**, 135 (1990).

[52] C. Chiccoli, O. D. Lavrentovich, P. Pasini, and C. Zannoni, Monte Carlo simulations of stable point defects in hybrid nematic films, Phys. Rev. Lett. **79**, 4401 (1997).

[53] C. Chiccoli, P. Pasini, L. R. Evangelista, R. Teixeira de Souza, and C. Zannoni, Lattice spin simulations of topological defects in nematic films with hybrid surface alignments, Int. J. Mod. Phys. C **22**, 505 (2011).

[54] C. Chiccoli, P. Pasini, C. Zannoni, G. Skačej, H. Yoshida, T. Hiroshima, K. Sunami, T. Ouchi, and M. Ozaki, From point to filament defects in hybrid nematic films, Sci. Rep. **9**, 17941 (2019).

[55] C. Chiccoli, P. Pasini, L. R. Evangelista, R. Teixeira de Souza, and C. Zannoni, Topological defects in nematic films between planar degenerate surfaces. A Monte Carlo study, Int. J. Mod. Phys. C **33**, 2250016 (2022).

[56] C. Chiccoli, P. Pasini, L. R. Evangelista, G. Skačej, R. Teixeira de Souza, and C. Zannoni, Elastic constants and the formation of topological defects in hybrid nematic cells: A Monte Carlo study, Phys. Rev. E **102**, 042702 (2020).

[57] G. R. Luckhurst and S. Romano, Computer simulation study of a nematogenic lattice model based on an elastic energy mapping of the pair potential, Liq. Cryst. **26**, 871 (1999).

[58] T. Gruhn and S. Hess, Monte Carlo simulation of the director field of a nematic liquid crystal with three elastic coefficients, Z. Naturforsch., Z. Naturforsch A **51**, 1 (1996).

[59] P. J. Le Masurier, G. R. Luckhurst, and G. Saielli, Monte Carlo lattice simulations of the elastic behaviour of nematic liquid crystals, Liq. Cryst. **28**, 769 (2001).

[60] P. A. Lebwohl and G. Lasher, Nematic liquid crystal order. A Monte Carlo calculation, Phys. Rev. A **6**, 426 (1972).

[61] U. Fabbri and C. Zannoni, Monte Carlo investigation of the Lebwohl–Lasher lattice model in the vicinity of its orientational phase transition, Mol. Phys. **58**, 763 (1986).

[62] G. Skačej and C. Zannoni, The nematic-isotropic transition of the Lebwohl-Lasher model revisited, Phil. Trans. R. Soc. A. **379**, 20200117 (2021).

[63] M. P. Allen and D. J. Tildesley, *Computer Simulation of Liquids*, 2nd ed. (Oxford University Press, Oxford, 2017).

[64] J. A. Barker and R. O. Watts, Structure of water; A Monte Carlo calculation, Chem. Phys. Lett. **3**, 144 (1969).

[65] D. A. Dunmur, Measurements of bulk elastic constants of nematics, in *Physical Properties of Liquid Crystals: Nematics*, edited by D. A. Dunmur, A. Fukuda, and G. R. Luckhurst (INSPEC-IEE, London, 2001)), pp. 216–229.